IIETA International Information and Engineering Technology Association
Advancing the World of Information and Engineering

Annales de Chimie - Science des Matériaux
Vol. 50, No. 1, February, 2026, pp. 87-97
Journal homepage: http://iieta.org/journals/acsm

Tailoring Pore Size in Clay Ceramics Using Cornstarch and Reduced Graphene Oxide as Pore-Forming Agents

Roquiya Laghrib[1,2], Abdallah Cheraitia[2*], Ikram Boukerche[1,3], Basma Al-Najar[4], Mohamed Bououdina[5,6]

[1] Department of Technology, Higher National School of Technological Education (ENSET), Skikda 21000, Algeria
[2] Laboratory of Silicate, Polymers and Nanomaterials (LSPN), University 8 Mai 194, Guelma 24000, Algeria
[3] Laboratory of Process Engineering for Sustainable Development and Health Products, National Polytechnic School of Constantine, Constantine 25000, Algeria
[4] Department of Physics, College of Science, University of Bahrain, Sakhir 32038, Bahrain
[5] Department of Mathematics and Sciences, College of Sciences and Humanities, Prince Sultan University, Riyadh 11586, Saudi Arabia
[6] Energy, Water and Environment Lab, College of Sciences and Humanities, Prince Sultan University, Riyadh 11586, Saudi Arabia

Corresponding Author Email: cheraitia.abdellah@univ-guelma.dz

https://doi.org/10.18280/acsm.500109

Received: 11 December 2025
Revised: 9 February 2026
Accepted: 17 February 2026
Available online: 28 February 2026

Keywords:
porous ceramics, starch porogen, reduced graphene oxide, clay materials, pore size control, eco-friendly

ABSTRACT

This study reports the development of low-cost porous ceramics derived from local clay materials, utilizing a synergistic combination of cornstarch and electrochemically exfoliated reduced graphene oxide (rGO) as dual pore-forming agents. Through an optimized processing route involving colloidal suspension preparation, slip casting, and controlled sintering at 1100 °C, macroscopically we developed intact ceramic membranes with tailored porosity. Comprehensive characterizations (X-ray diffraction (XRD), scanning electron microscopy with energy-dispersive X-ray spectroscopy (SEM-EDS), Brunauer-Emmett-Teller (BET), thermogravimetric analysis (TGA), and Fourier transform infrared spectroscopy (FTIR)) revealed a predominant quartz-cristobalite matrix (approx. 85%), while carbon residues were below the detection limits of the EDS system following oxidative sintering. The textural properties varied significantly across the five samples: while the starch-dominated matrices exhibited partial vitrification and low specific surface areas (≈ 3.53–3.62 m^2/g), the rGO-stabilized samples (S3 and S4) retained a robust mesoporous framework with surface areas reaching up to 59.51 m^2/g. Nitrogen adsorption isotherms for the macroporous samples showed a rapid increase in volume near saturation (P/P0 > 0.90), indicating high pore volumes (up to 1.69 cm^3/g). Conversely, the rGO-enriched samples maintained calibrated pore diameters in the 4.3–5.6 nm range. This dual porogen approach achieves a total porosity of 45–65% while preserving structural integrity, offering a sustainable and cost-effective route for advanced applications in catalytic supports and water filtration.

1. INTRODUCTION

Porous ceramics offer excellent properties due to their high porosity, facilitating interactions with atoms, ions, and molecules through complex, tailorable pore structures for applications in filtration, adsorption, and biomedicine [1, 2].

Recent studies highlight natural minerals (kaolin, bentonite, feldspar) for porous ceramics due to their abundance, high melting point, mechanical strength, thermal stability, and chemical resistance [3-7]. These enhance performance in filtration membranes, thermal insulation, construction materials, and catalyst supports [3, 6, 8-10].

The pore-forming agent (PFA) method is the most commonly used fabrication technique, mainly because it's simple and cost-effective in creating porosity via combustible additives (starch, graphite, lycopodium, sucrose, polymethyl methacrylate, polypropylene, and carbon black) [11] that burn out during sintering [7, 12-18]. Microstructure-related parameters such as porosity, pore size, shape, distribution, and connectivity contribute to the performance of porous ceramics, depending on the requirements of the corresponding application [8, 13]. Cornstarch provides clean burnout and affordability but variable pore size due to swelling [17, 19-22]. Graphite produces uniform small pores at 600-850 °C without liquid phase shrinkage [7, 23-25], while reduced graphene oxide (rGO) offers a promising alternative [26-28].

While cornstarch creates massive macropore networks (ideal for high-flux fluid transport) and rGO generates fine micro/mesoporosity and thermal scaffolding, the synergistic combination of these two agents in local clay matrices remains unexplored. There is a critical lack of studies addressing how a bimodal (micro-macro) pore network can be tailored using cost-effective local resources while maintaining structural integrity at high temperatures [29, 30].

This study addresses this gap by reporting a novel porous ceramic material that integrates both rGO and Cornstarch into

a local clay-based ceramic. By combining slip-casting with this dual-PFA approach, we aim to design a bimodal pore structure where rGO acts as a nanoscale scaffold preventing clay vitrification, while cornstarch provides high volumetric macroporosity. The objective of this paper is to evaluate the influence of varying rGO and CS contents on pore morphology, size distribution, mineralogical transformations, and thermal behavior, thereby optimizing local clay composites for advanced water filtration applications.

2. MATERIALS AND METHODS

We prepared porous ceramic membranes using slip casting technique. A homogeneous mixture was obtained by combining the prepared slip with pore-forming agents, which was then poured into plaster molds. After draining the excess slip, the samples were dried at room temperature to ensure uniform evaporation and prevent cracking. This was followed by a thermal treatment process at 1100 °C to remove residual water and harden the structure.

2.1 Preparation of the liquid suspension

The liquid suspension was fabricated with five raw materials, namely Hycast VC clay, a mixture of kaolins (Tamazert, Remblend and LPC), feldspar, quartz, and a mixture of sodium silicate and sodium carbonate as binders; these materials were purchased from the sanitary ceramic factory of El-milia-Jijel, Algeria. The preparation steps of the liquid suspension are shown in Figure 1.

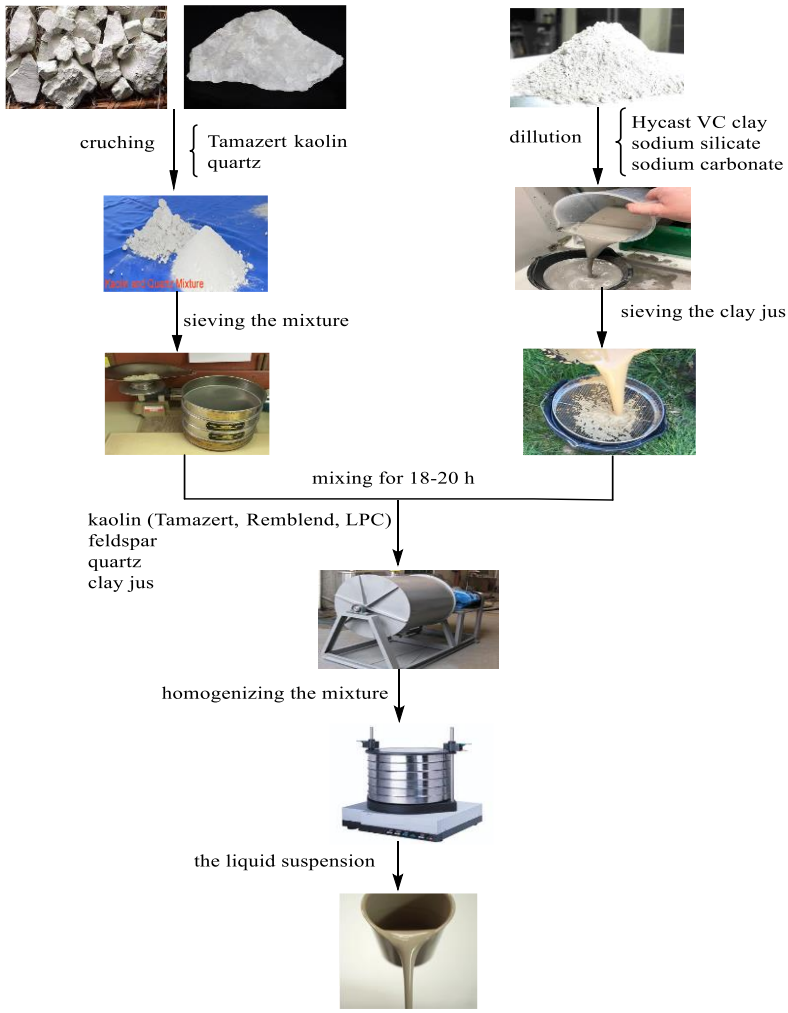

Figure 1. Preparation process of the liquid suspension

2.2 Preparation of reduced graphene oxide by electrochemical exfoliation

rGO is produced electrochemically by exfoliating graphite in an electrolytic KOH solution (1 M concentration) by applying an 8–10 voltage between graphite electrodes spaced 2 cm apart for one hour. Following the electrochemical exfoliation, the resulting dispersions were subjected to an ultrasonic treatment for one hour. In a filtration system, successive washes were carried out with distilled water and a HCl 1M solution, and the residuals were then washed thoroughly with deionized water using vacuum filtration. The particles were vacuum-dried for two hours at 100 °C.

Based on the polarization of graphitic layers by OH ions, the electrochemical exfoliation process suggests the following reactions to occur on the electrodes:

- At the cathode: $4H_2O + 4e^- \rightarrow 2H_2(g) + 4OH^-$
- At the anode: $4OH^- \rightarrow O_2(g) + 2H_2O + 4e^-$

As shown in Figure 2(a), instead of the expansion introduced by gas formation, exfoliation is caused by the electrostatic interaction of the graphitic layers with the OH- ions moving under the influence of the applied electric field

and its oxidation to O_2 gas [31].

2.3 Preparation of porous ceramic membranes

Commercially available cornstarch was purchased from a local shop used with rGO powders as pore forming agents in the ceramic samples.

Pore-forming agents (Cornstarch and Cornstarch/ rGO mixture) with different weight contents were added to the liquid suspension. Details of membrane samples compositions are provided in Table 1.

The slip was poured into the plaster mold after aging for 24 hours, water was absorbed into the mold by capillary action, generating a layer of clay to build up inside the plaster mold.

After draining the excess slip, the cast was partially air-dried in the mold (Figure 2(b)). The resulting green bodies were then oven-dried at 60 °C for 24 hours to ensure complete moisture removal.

The samples were subsequently sintered in a muffle furnace, strictly following the ceramic fabrication protocol and the specific temperature profile illustrated in Figure 2(c).

Table 1. Pore-forming agent content (wt. %) and deposit time of the prepared samples

Specimen No.	Slip	Cornstarch (wt. %)	rGO (wt. %)	Contact Time(min)
S1	Reference	0	0	2
S2	1layer	4	0	2
S3	1 layer	4	1	2
S4	3 layers	4:0:4	0:2:0	1/layer

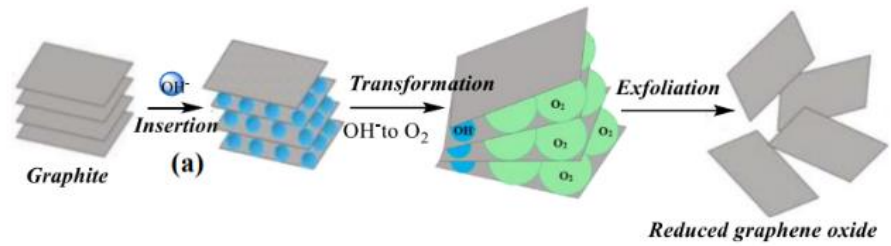

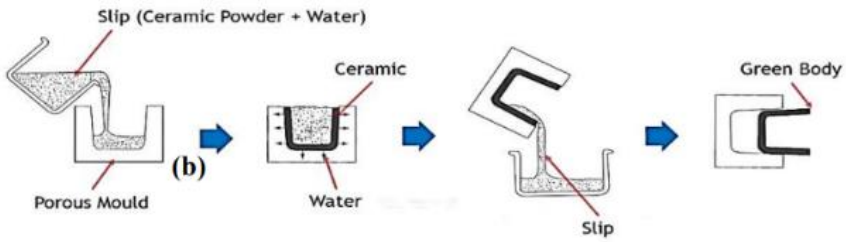

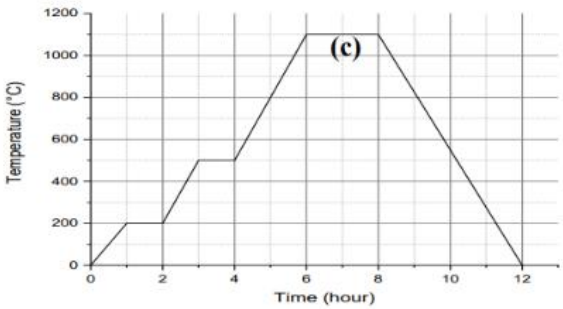

Temperature	Rate (°/min))
0-200	3
200-500	3
500-1100	5
1100	For 120 min
1100-ambiant	10

Figure 2. Process flow and experimental protocols: (a) graphite electrochemical exfoliation; (b) fabrication process of ceramic samples via slip casting; (c) sintering cycle

2.4 Characterization

The surface morphology of the sintered samples was analyzed by scanning electron microscopy (SEM; Thermo Scientific Quattro S) coupled with energy-dispersive X-ray spectroscopy (EDS) at an accelerating voltage of 5 kV and working distances ranging from 2.5 to 10 µm, enabling simultaneous examination of surface morphology and local chemical composition. The properties of the prepared porous ceramics were investigated using different techniques. Elemental analysis of the prepared samples was determined by total reflection X-ray fluorescence spectroscopy (TXRF; KLA Tencor D500 and Rigaku ZSX Primus IV). Phase identification of the sintered specimens was performed by X-ray diffraction (XRD) (Bruker D8 ADVANCE, Bragg-Brentano configuration) using Cu-Kα radiation (λ = 1.5406 Å) over a 2θ range of 5-90° at room temperature. Chemical characteristics of graphene powders were performed by Fourier transform infrared spectroscopy (FTIR-ATR; IRAffinity-1S, Shimadzu) in the range of 400 - 4000 cm^{-1}.

Textural properties, including porosity and pore size distribution of specimens sintered at 1100 °C, were quantified

through Brunauer-Emmett-Teller (BET) analysis of nitrogen adsorption–desorption isotherms (QUANTQCHROME AUTOSORB IQ3 analyzer).

Differential scanning calorimetry (DSC) of graphene powders was performed using a Mettler Toledo thermal analyzer (Switzerland) from 35 to 600 ℃ under air flow. Additionally, the thermal degradation behavior of the green specimens was characterized by thermogravimetric analysis (TGA) using the same equipment. TGA measurements were conducted under a nitrogen atmosphere at a heating rate of 10 ℃/min, covering a temperature range from 25 to 1200 ℃.

3. RESULTS AND DISCUSSION

3.1 Chemical composition of the membranes

X-ray fluorescence spectrometry analysis of the dried slip powder (Table 2) indicates a predominantly silico-aluminous composition, with SiO_2 (65.65%) and Al_2O_3 (19.98%) constituting the major phases. Trace components (K_2O, Na_2O, Fe_2O_3, TiO_2, CaO, MgO) and carbon content collectively account for less than 7% of the total composition, with individual concentrations ranging from 0.16% to 2.25%.

Table 2. Chemical composition of the prepared ceramic suspension (wt. %)

Oxides	SiO_2	Al_2O_3	TiO_2	Fe_2O_3	CaO	MgO	K_2O	Na_2O	C	PF
Weight%	65,65	19,98	0.31	0.57	0.25	0.16	2.25	1.30	0.55	5.53

3.2 Morphological and elemental analysis (Scanning electron microscopy with energy-dispersive X-ray spectroscopy)

Microstructural analysis via SEM of the developed ceramic membranes—S1 (Reference), S2 (Single layer with CS), and S4 (Three layers)—is presented in Figure 3(a-c). The interfacial regions and the distinct multi-layered morphology of the specimens are highlighted in Figure 3(d). Furthermore, Figure 3(e) reveals continuous surfaces with no apparent cracking and a well-defined porous architecture, which was further quantified using BET surface area and porosity analysis.

Additionally, Energy Dispersive Spectroscopy (EDS) was employed to characterize the elemental distribution within the ceramic matrix. The inlets in Figure 3(a-c) illustrate the cross-sectional mapping of the selected areas, confirming the presence of key constituent elements: Al, Si, Ca, Ti, O, and Zr.

Notably, carbon was not detected in the sintered samples, suggesting the near-complete decomposition of rGO templates during air-sintering. While rGO directs the structure in the initial stages, any residual carbon after treatment at 1100 °C likely fell below the standard EDS detection limit (0.1–0.5 wt%) [32, 33].

This observation is consistent with the high-temperature oxidation of carbon nanomaterials in oxygen-rich environments, resulting in a refined, carbon-free ceramic framework. Consequently, the EDS and SEM results confirm the successful fabrication of these novel porous membranes, demonstrating significant potential for diverse applications, including catalysis, composite preforms, porous electrodes, and advanced filtration technologies [25, 34].

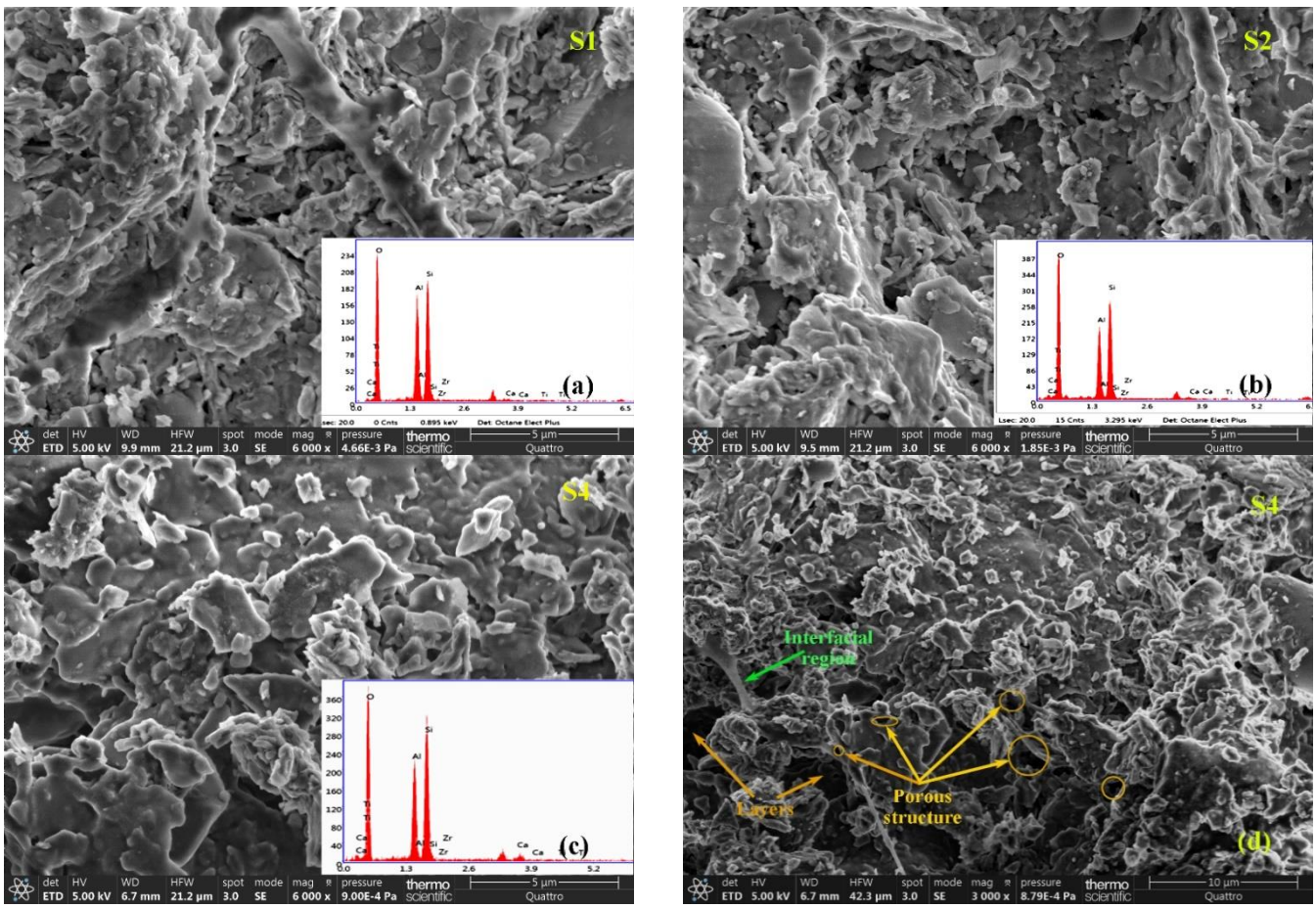

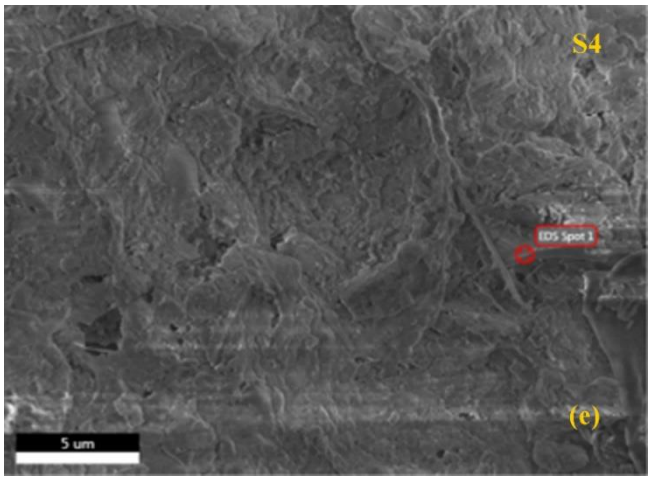

Figure 3. SEM micrographs and EDS analysis of the ceramic samples: (a) surface morphology of the reference sample S1; (b) surface morphology of the 1-layer rGO sample S2; (c) surface morphology of the 2-layer rGO sample S4; (d) surface structure of the 2-layer rGO sample S4; (e) EDS elemental mapping of the 2-layer rGO sample S4

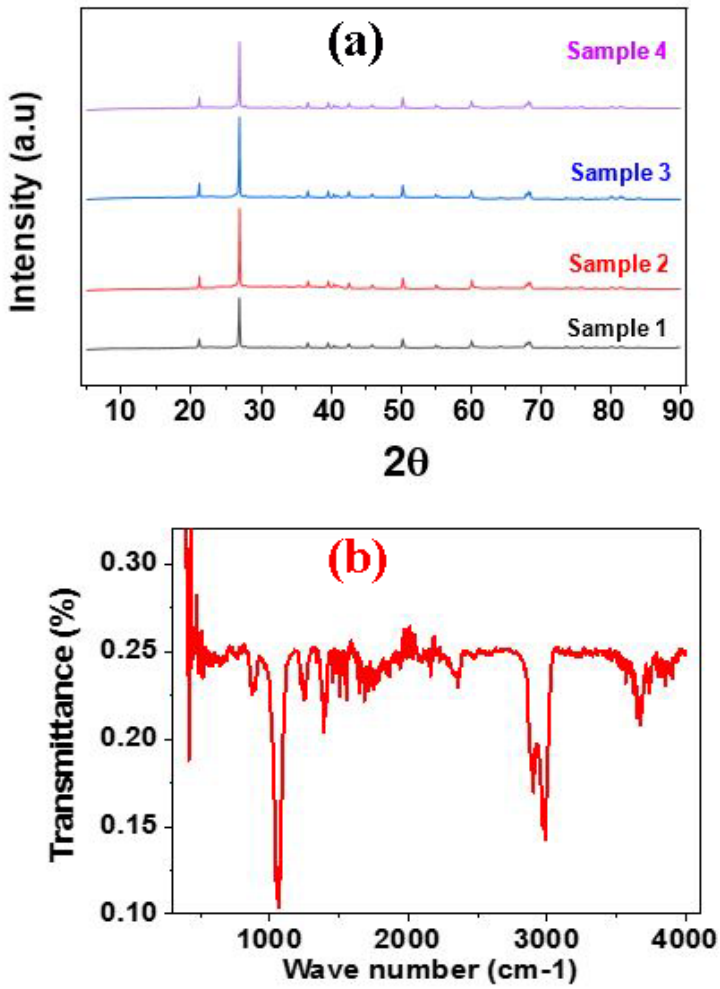

Figure 4. Structural and phase characterization: (a) X-ray diffraction (XRD) patterns of the fabricated ceramic membranes; (b) Fourier transform infrared spectroscopy (FTIR) spectrum of reduced graphene oxide (rGO) powder

3.3 Crystalline and physicochemical properties of the ceramic membranes

The crystal structure of the ceramics membranes was confirmed by XRD. All peaks are consistent with the ceramic crystalline phase as shown in Figure 4 (a). The sample treated at 1100 ℃ consists predominantly of quartz (60%), as confirmed by its characteristic XRD peaks at 26.6° (d = 3.34 Å), 20.8°, and 50.1°. Cristobalite (25%), a high-temperature polymorph of silica formed by the thermal transformation of quartz), is identified by its distinct peak at 21.9° (d = 4.05 Å). The feldspar albite (10%) remains thermally stable under these

conditions, showing diagnostic reflections at 22.0° and 27.9°. A minor component of residual muscovite (~5%) persists, indicated by a weak 8.8° (10.0 Å) basal reflection, suggesting incomplete dihydroxylation [35, 36].

Amorphous phases such as K-Al-Si glass and nanocrystalline γ-Al_2O_3 might be present, but their detection by XRD is challenging due to the technique's limitations in identifying non-crystalline structures and nanoscale materials.

FTIR analysis was carried out to confirm the physicochemical structure of rGO powders. In FTIR spectrum in Figure 4(b), the rGO exhibited the absorption band at 3670 cm^{-1} corresponding to free O–H stretching [37]. Two large peaks were detected at 2978 cm^{-1} and 2897 cm^{-1} attributed to C-H asymmetric and symmetric stretching [38]. Further, the band at 1396 cm^{-1} is assigned to the O–H deformation, the C–OH stretching at 1238 cm^{-1} and C–O vibration at 1062 cm^{-1}, revealing the presence of epoxy and alkoxy groups respectively, which were the result of interaction between rGO and remnant water [37, 39, 40].

The peak observed at 879 cm-1is expected to be for the bending vibrations of the C–H bond [41].

3.4 Surface characterization and pore structure of the ceramic slips

The analysis of the nitrogen adsorption-desorption isotherms reveals two distinct textural behaviors governed by the concentration of pore-forming agents and the resulting pore architecture:

As illustrated in Figure 5, increasing cornstarch concentrations significantly enhances the total pore volume within the ceramic structure [42]. Conversely, higher rGO content results in a shift in the textural profile. Although rGO undergoes thermal oxidation between 575–775 °C [23], it acts as a fugitive structural directing agent (SDA). By intercalating within the clay matrix during the green state, the rGO nanosheets create a network of fine mesopores that persist as a "footprint" after sintering. This mechanism is responsible for the dramatic increase in specific surface area, rising from 3.53 m^2/g in the reference (S1) to over 50 m^2/g in the rGO-modified samples (S3, S4).

In Table 3, S3 and S4 exhibit Type IV isotherms with H2b-type hysteresis loops according to the International Union of Pure and Applied Chemistry (IUPAC) classification. This profile is characteristic of mesoporous materials [43, 44] featuring complex, interconnected networks often associated with "ink-bottle" pore geometries [36, 45-50]. This bimodal connectivity—where macropores from cornstarch are linked by rGO-derived mesopores—is ideal for high-flux fluid transport combined with high internal surface area.

In contrast, S1 and S2 show negligible nitrogen uptake at low relative pressures, followed by a sharp increase in adsorbed volume near saturation (P/P0 > 0.9). This behavior is typical of macroporous materials where the internal surface area is low due to partial vitrification of the local clay at 1100 °C. In these reference samples, fine pores collapse or fuse into large macropores with smooth internal walls. However, the presence of rGO in S3 and S4 appears to inhibit this total vitrification by acting as a temporary physical barrier at grain boundaries, thereby preserving the mesoporous framework.

The results highlight the critical influence of the 1100 °C thermal treatment on the pore structure:

1. For the samples (S1, S2), the low specific surface area values (≈3.5 to 3.6 m^2/g) are attributed to the partial vitrification of the local clay matrix. At high temperatures, fine pores (micro and mesopores) collapse or fuse into large macropores. While the surface area decreases, the pore volume remains high (>1.2 cm^3/g), indicating a highly open structure with smooth internal walls [51].

2. In contrast, the samples (S3, S4) maintained a stable mesoporous network, with surface areas exceeding 50 m^2/g. This textural stability is vital for fine filtration or catalytic applications, providing a larger interface for contact [30].

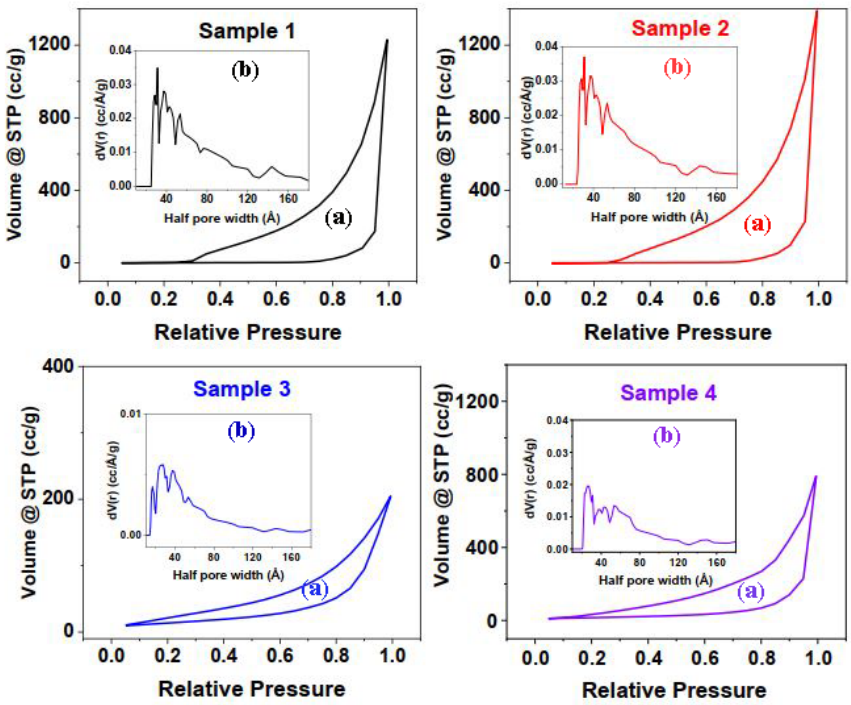

Figure 5. Porous structure characterization: (a) nitrogen adsorption-desorption isotherms; (b) pore size distribution of the ceramic samples

Table 3. Structural characteristics of the ceramic samples (Multi-point BET model)

Sample	Specific Surface Area (m^2/g)	Pore Volume (cm^3/g)	Dominant Profile
S1	3.53	1.23	Macroporous
S2	3.62	1.39	Macroporous
S3	51.02	0.26	Mesoporous
S5	59.51	0.79	Mesoporous

To ensure scientific consistency and rigor, the Multi-Point BET (MBET) method was exclusively used to determine the specific surface area. Pore-filling models (such as Barrett-Joyner-Halenda (BJH) or Density Functional Theory (DFT)) were discarded for surface area comparison to avoid mathematical artifacts related to capillary condensation or fitting errors caused by the irregular morphology of natural clay pores.

3.4.1 Thermogravimetric and differential thermal analysis

In Figure 6, the DSC analysis shows the thermograph of rGO. The first endothermal peak appearing at 85 ℃ is attributed to the elimination of adsorbed water molecules and the decomposition of the more labile oxygen functional groups [40, 52, 53]. At about 565 ℃ a second peak appeared, which corresponds to the beginning of the thermal degradation of graphene (the graphene sample burned up with some residue impurities) [53, 54].

Figure 6 presents the thermal behavior of untreated samples, revealing four distinct degradation stages: (1) Initial moisture evaporation (0.25% mass loss at 156 ℃) [21], evidenced by an endothermic peak at 100 ℃ [55]; (2) A minor mass gain (156-300 ℃) attributed to oxidation of Fe/Mg-containing clay minerals; (3) Significant dehydroxylation of kaolinite between 400-600°C (4.5% mass loss) [21, 54, 55], ($Al_2O_3 \cdot 2SiO_2 \cdot 2H_2O \rightarrow Al_2O_3 \cdot 2SiO_2$) accompanied by an exothermic peak at 550°C from hydroxyl group expulsion [3, 55]; and (4) Final decomposition of carbonaceous materials (>600 ℃, 1% mass loss) [56] with γ-alumina formation indicated by an 850 ℃ exothermic peak [55]. Panels (b) and (c) reproduce these transitions while revealing additional starch decomposition at 300 ℃ [55, 56].

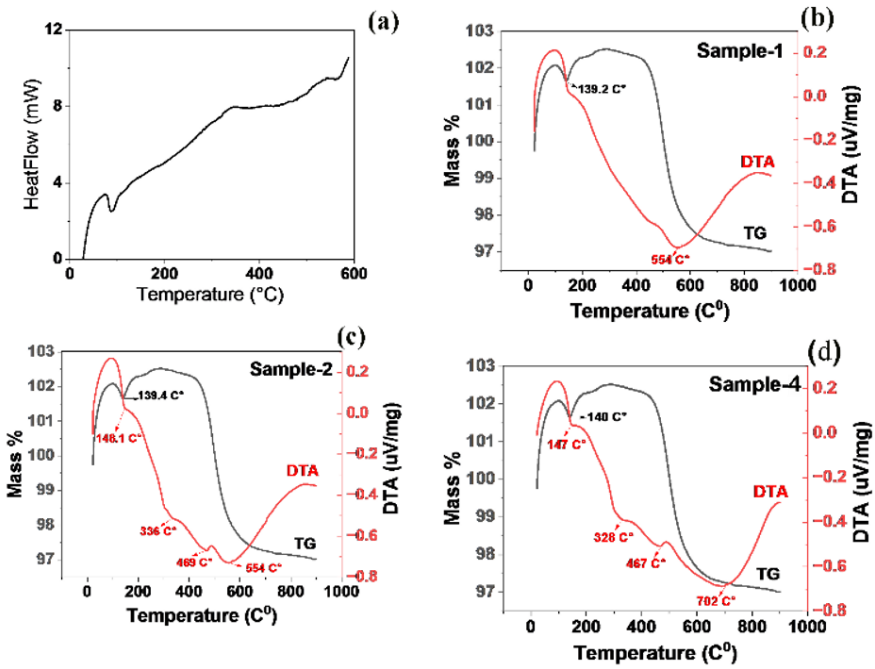

Figure 6. Thermal analysis of the materials: (a) DSC thermogram of reduced graphene oxide (rGO) powder; (b–d) TGA/DTA curves of ceramic samples S1, S2, and S4, respectively

Note: DSC: Differential Scanning Calorimetry; TGA: Thermogravimetric Analysis; DTA: Differential Thermal Analysis.

3.5 Comparative study

The strategies for generating porosity in ceramic materials vary significantly based on the choice of pore-forming agents and sintering parameters, as summarized in Table 4.

Recent research has highlighted a variety of strategies for generating porosity, each offering distinct advantages. Alvarado et al. [57] demonstrated that cornstarch in diatomite-based ceramics achieves high porosity (59.3%) but noted a significant trade-off with mechanical strength. Similarly, Salman et al. [58] and Nie and Lin [9] explored organic wastes, confirming that the agent's nature dictates permeability and connectivity.

In alumina systems, the combination of graphite and starch has been shown to produce balanced microstructures [7, 59]. While graphite facilitates high porosity through complete oxidation at lower temperatures, starch ensures stable interconnectivity at elevated temperatures. More advanced hierarchical structures have been achieved using corn stalks [60].

Moving beyond single-agent pore generation, Biggemann et al. [61] and Nasir et al. [62] explored the use of organic microspheres, natural fibers, yeast, and expandable polymeric spheres (EPS). These studies demonstrated that the choice and size of pore-forming agents can be tailored to engineer multimodal pore size distributions, optimizing properties like

permeability, strength, and thermal conductivity for specific applications.

Most recently, Zhao et al. [63] presented a direct foaming method for fabricating porous SiC ceramics. This technique utilizes hydrogen peroxide (H_2O_2) as a foaming agent, generating oxygen bubbles that form primary macropores (0.5–3 mm), while the packing of SiC particles creates secondary pores (~2 μm).

Our study introduces a novel approach using local clay combined with cornstarch and rGO. Unlike traditional methods that often result in purely macroporous structures at 1100 °C, the synergistic effect of rGO sheets and ceramic particles allowed for the retention of a significant mesoporous network.

While previous literature on starch-based ceramics often focuses on macro-scale voids, our membranes achieved specific surface areas reaching 59.51 m^2/g with precisely controlled mesopores in the 4.3–5.6 nm range. This performance is particularly noteworthy given the high sintering temperature, which typically induces vitrification and surface area loss in clay-based materials. By avoiding common mathematical artifacts such as the Tensile Strength Effect (TSE), we confirmed that our rGO-stabilized ceramics offer superior surface-to-volume ratios compared to standard clay-starch formulations, making them highly suitable for advanced filtration and adsorption applications.

Table 4. Comparative table of porosity generation techniques in ceramic materials

Base Material	Pore-Forming Agent	Sintering Temp (°C)	Porosity (%)	Pore Size	Author(s) & Year
Diatomite	Cornstarch	1150	Up to 59.28	Interconnected	[58]
Alumina	Graphite waste	>600	37.3-61.1	Interconnected	[61]
Alumina	Starch	1300	>50	Small micropores	[62]
Alumina	Graphite	1100	66	Larger pores	[62]
Alumina	Starch + Graphite	1300	Moderate	Mixed (small + large)	[62]
Alumina	Cornstarch	Not specified	14.8-55.3	Network of pores	[60]
Secondary aluminum dross	Corn stalks	Not specified	0.58 cm^3/g 174.83 m^2/g	Hierarchical (micro/nano)	[63]
Kaolin + feldspar	Cornstarch	1200	26.3	Fine, uniform	[59]
Kaolin + feldspar	Paper waste	1200	19.1	Intermediate	[59]
Kaolin + feldspar	Sawdust	1200	Lower	Larger	[59]
Anorthite	Banana peel	Not specified	~45 (open)	Not specified	[5]
Alumina	Organic microspheres, fibers, starch	Not specified	Not specified	Multimodal	[61]
Alumina-zeolite-CaO	Yeast	1400	Not specified	Up to 402 μm	[62]
Alumina-zeolite-CaO	Al powder/EPS	Not specified	Not specified	Variable	[62]
SiC	H_2O_2 + SDS	Not specified	Hierarchical	0.5-3 mm + ~2 μm	[63]
Local clay	Cornstarch + rGO	1100	Controlled 3.5 – 59.5 m^2/g	Mesoporous (4–6 nm)	Our Study

Note: EPS = Expanded Polystyrene; SDS = Sodium Dodecyl Sulfate; rGO = Reduced Graphene Oxide.

4. CONCLUSIONS

This study presents an eco-friendly route for fabricating porous ceramic membranes from local clay, using a dual-porogen system of cornstarch and electrochemically exfoliated rGO.

Microstructural analysis confirmed the formation of morphologies with no apparent cracking, while textural characterization revealed a predominantly mesoporous network. By employing MBET model, average pore diameters were precisely determined between 4.3 and 5.6 nm. The incorporation of rGO was critical in tailoring the pore architecture; synergistic interactions between 2D rGO nanosheets and the ceramic matrix effectively stabilized the mesoporous framework against high-temperature sintering at 1100 °C.

The samples showed significant structural variations: while starch-modified samples (S1, S2) exhibited macroporous behavior (1.39 cm^3/g) but low surface areas due to vitrification. rGO-loaded samples (S3, S4) retained high specific surface areas (59.51 m^2/g).

This dual-agent approach allows for superior control over pore hierarchy compared to traditional methods. The ability to tailor porosity—from transport macropores to high-surface-area mesopores—renders these membranes highly versatile for advanced water purification, gas separation, and catalysis applications.

REFERENCES

[1] Sooksaen, P., Karawatthanaworrakul, S. (2015). The properties of Southern Thailand clay-based porous ceramics fabricated from different pore size templates. Applied Clay Science, 104: 295-302. https://doi.org/10.1016/j.clay.2014.12.009

[2] Jahandideh, H., Macairan, J.R., Bahmani, A., Lapointe, M., Tufenkji, N. (2022). Fabrication of graphene-based porous materials: Traditional and emerging approaches. Chemical Science, 13(31): 8924-8941. https://doi.org/10.1039/D2SC01786E

[3] Mouiya, M., Bouazizi, A., Abourriche, A., Benhammou, A., El Hafiane, Y., Ouammou, M., Abouliatim, Y., Younssi, S.A., Smith, A., Hannache, H. (2019). Fabrication and characterization of a ceramic membrane from clay and banana peel powder: Application to industrial wastewater treatment. Materials Chemistry and Physics, 227: 291-301. https://doi.org/10.1016/j.matchemphys.2019.02.011

[4] Addich, M., El Baraka, N., Saffaj, N., Laknifli, A., Karim, A., Sbihi, K., El Hammadi, A. (2022). Elaboration of innovative ceramic microfiltration

membrane from natural Moroccan sand for wastewater treatment. Desalination and Water Treatment, 260: 299-308. https://doi.org/10.5004/dwt.2022.28550

[5] Hua, K., Shui, A., Xu, L., Zhao, K., Zhou, Q., Xi, X. (2016). Fabrication and characterization of anorthite–mullite–corundum porous ceramics from construction waste. Ceramics International, 42(5): 6080-6087. https://doi.org/10.1016/j.ceramint.2015.12.165

[6] Deng, X., Zhang, W., Yin, J., Deng, C., Zhang, S., Zhang, H., Ran, S. (2020). Microstructure and mechanical performance of porous mullite ceramics added with TiO2. Ceramics International, 46(6): 8438-8443. https://doi.org/10.1016/j.ceramint.2019.12.078

[7] Ali, M.S., Hanim, M.A.A., Tahir, S.M., Jaafar, C.N.A., Norkhairunnisa, M., Matori, K.A. (2017). Preparation and characterization of porous alumina ceramics using different pore agents. Journal of the Ceramic Society of Japan, 125(5): 402-412. https://doi.org/10.2109/jcersj2.16233

[8] Çelik, A., Çağlar, G., Çelik, Y. (2022). Fabrication of porous Al2O3 ceramics using carbon black as a pore forming agent by spark plasma sintering. Ceramics International, 48(19): 28181-28190. https://doi.org/10.1016/j.ceramint.2022.06.121

[9] Nie, Z., Lin, Y. (2015). Fabrication of porous alumina ceramics with corn starch in an easy and low-cost way. in Proceedings of the 2015 International Conference on Mechanics, Materials and Manufacturing. https://www.ceramics-silikaty.cz/2015/pdf/2015_04_348.pdf.

[10] Bai, J. (2010). Fabrication and properties of porous mullite ceramics from calcined carbonaceous kaolin and α-Al_2O_3. Ceramics International, 36(2): 673-678. https://doi.org/10.1016/j.ceramint.2009.10.006

[11] Jalaluddin, M.L., Azlan, U.A.A., Abd Rashid, M.W., Tamin, N., Masri, M.N. (2024). A review of pore-forming agents on the structures, porosities, and mechanical properties of porous ceramics. AIMS Materials Science, 11(4): 634-665. https://doi.org/10.3934/matersci.2024033

[12] Zhang, F.Z., Kato, T., Fuji, M., Takahashi, M. (2006). Gelcasting fabrication of porous ceramics using a continuous process. Journal of the European Ceramic Society, 26(4-5): 667-671. https://doi.org/10.1016/j.jeurceramsoc.2005.07.021

[13] Liu, R., Xu, T., Wang, C.A. (2016). A review of fabrication strategies and applications of porous ceramics prepared by freeze-casting method. Ceramics International, 42(2): 2907-2925. https://doi.org/10.1016/j.ceramint.2015.10.148

[14] Alghamdi, H., Dakhane, A., Alum, A., Abbaszadegan, M., Mobasher, B., Neithalath, N. (2018). Synthesis and characterization of economical, multi-functional porous ceramics based on abundant aluminosilicates. Materials & Design, 152: 10-21. https://doi.org/10.1016/j.matdes.2018.04.060

[15] Xu, G., Ma, Y., Cui, H., Ruan, G., Zhang, Z., Zhao, H. (2014). Preparation of porous mullite–corundum ceramics with controlled pore size using bioactive yeast as pore-forming agent. Materials Letters, 116: 349-352. https://doi.org/10.1016/j.matlet.2013.11.067

[16] Dele-Afolabi, T.T., Azmah Hanim, M.A., Ojo-Kupoluyi, O.J., Calin, R., Zuhri, M.Y.M. (2021). Tailored pore structures and mechanical properties of porous alumina ceramics prepared with corn cob pore-forming agent. International Journal of Applied Ceramic Technology, 18(1): 244-252. https://doi.org/10.1111/ijac.13621

[17] Obada, D.O., Dodoo-Arhin, D., Dauda, M., Anafi, F.O., Ahmed, A.S., Ajayi, O.A. (2017). The impact of kaolin dehydroxylation on the porosity and mechanical integrity of kaolin based ceramics using different pore formers. Results in Physics, 7: 2718-2727. https://doi.org/10.1016/j.rinp.2017.07.048

[18] Pia, G., Casnedi, L., Sanna, U. (2015). Porous ceramic materials by pore-forming agent method: An intermingled fractal units analysis and procedure to predict thermal conductivity. Ceramics International, 41(5): 6350-6357. https://doi.org/10.1016/j.ceramint.2015.01.069

[19] Li, S., Wang, C.A., Zhou, J. (2013). Effect of starch addition on microstructure and properties of highly porous alumina ceramics. Ceramics International, 39(8): 8833-8839. https://doi.org/10.1016/j.ceramint.2013.04.072

[20] Wu, C., Li, Z., Li, Y., Wu, J., Zhao, Y., Liao, Y. (2023). Effect of starch on pore structure and thermal conductivity of diatomite-based porous ceramics. Ceramics International, 49(1): 383-391. https://doi.org/10.1016/j.ceramint.2022.08.352

[21] Elomari, H., Achiou, B., Karim, A., Ouammou, M., Albizane, A., Bennazha, J., Younssi, S.A., Elamrani, I. (2017). Influence of starch content on the properties of low cost microfiltration membranes. Journal of Asian Ceramic Societies, 5(3): 313-319. https://doi.org/10.1016/j.jascer.2017.06.004

[22] Bazin, M.M., Ahmat, M.A., Zaidan, N., Ismail, A.F., Ahmad, N. (2014). Effect of starch addition on microstructure and strength of ball clay membrane. Jurnal Teknologi (Sciences & Engineering), 69(9). https://doi.org/10.11113/jt.v69.3408

[23] Deheria, S. (2014). Production of alumina based porous ceramics using graphite powder as the pore former. http://ethesis.nitrkl.ac.in/6086/1/e-204.pdf.

[24] Li, Q., Ma, F. (2012). Study on the dispersion of graphite as pore former. Advanced Materials Research, 412: 370-373.https://doi.org/10.4028/www.scientific.net/AMR.412.370

[25] Ding, S., Zhu, S., Zeng, Y.P., Jiang, D. (2007). Fabrication of mullite-bonded porous silicon carbide ceramics by in situ reaction bonding. Journal of the European Ceramic Society, 27(4): 2095-2102. https://doi.org/10.1016/j.jeurceramsoc.2006.06.003

[26] Pei, S., Cheng, H.M. (2012). The reduction of graphene oxide. Carbon, 50(9): 3210-3228. https://doi.org/10.1016/j.carbon.2011.11.010

[27] Compton, O.C., Nguyen, S.T. (2010). Graphene oxide, highly reduced graphene oxide, and graphene: Versatile building blocks for carbon-based materials. Small, 6(6): 711-723. https://doi.org/10.1002/smll.200901934

[28] Eigler, S., Hirsch, A. (2014). Chemistry with graphene and graphene oxide—challenges for synthetic chemists. Angewandte Chemie International Edition, 53(30): 7720-7738. https://doi.org/10.1002/anie.201402780

[29] Lyckfeldt, O., Ferreira, J.M.F. (1998). Processing of porous ceramics by 'starch consolidation'. Journal of the European Ceramic Society, 18(2): 131-140. https://doi.org/10.1016/S0955-2219(97)00101-5

[30] Walker, L.S., Marotto, V.R., Reif, J., Koratkar, N.,

Corral, E.L. (2011). Toughening in graphene ceramic composites. ACS nano, 5(4): 3182-3190. https://doi.org/10.1021/nn200319d

[31] Raj, C.J., Manikandan, R., Thondaiman, P., Sivakumar, P., Savariraj, A.D., Cho, W.J., Kim, B.C., Jung, H. (2021). Sonoelectrochemical exfoliation of graphene in various electrolytic environments and their structural and electrochemical properties. Carbon, 184: 266-276. https://doi.org/10.1016/j.carbon.2021.08.027

[32] Goldstein, J.I., Newbury, D.E., Michael, J.R., Ritchie, N.W., Scott, J.H.J., Joy, D.C. (2018). Scanning Electron Microscopy and X-Ray Microanalysis (4e ed.). Springer. https://doi.org/10.1007/978-1-4939-6676-9

[33] Shalaby, A.S.A., Staneva, A.D., Aleksandrov, L.I., Iordanova, R.S., Dimitriev, Y.B. (2016). Preparation, characterization and thermal stability of reduced graphene oxide/silicate nanocomposite. Bulgarian Chemical Communications, 48(1): 38-42.

[34] Qi, T., Chen, X., Fan, Y., Zhong, J. (2025). Ceramic membrane technology for the separation and purification of bioactive compounds: A critical review of applications, diafiltration modeling, and fouling prevention. Separation and Purification Technology, 361: 131301. https://doi.org/10.1016/j.seppur.2024.131301

[35] Lafuente, B., Downs, R.T., Yang, H., Stone, N. (2015). 1. The power of databases: The RRUFF project. In Highlights in Mineralogical Crystallography, pp. 1-30. https://doi.org/10.1515/9783110417104-003

[36] Heller-Kallai, L., Lapides, I. (2015). Dehydroxylation of muscovite: Study of quenched samples. Physics and Chemistry of Minerals, 42(10): 835-845. https://doi.org/10.1007/s00269-015-0767-4

[37] Zhao, Y., Zhan, L., Tian, J., Nie, S., Ning, Z. (2011). Enhanced electrocatalytic oxidation of methanol on Pd/polypyrrole–graphene in alkaline medium. Electrochimica Acta, 56(5): 1967-1972. https://doi.org/10.1016/j.electacta.2010.12.005

[38] Prusty, K., Barik, S., Swain, S.K. (2019). A corelation between the graphene surface area, functional groups, defects, and porosity on the performance of the nanocomposites. Functionalized Graphene Nanocomposites and their Derivatives, 2019: 265-283. https://doi.org/10.1016/B978-0-12-814548-7.00013-1

[39] Chu, K.H., Fathizadeh, M., Yu, M., Flora, J.R., Jang, A., Jang, M., Jang, M., Park, C.M., Yoo, S.S., Her, N., Yoon, Y. (2017). Evaluation of removal mechanisms in a graphene oxide-coated ceramic ultrafiltration membrane for retention of natural organic matter, pharmaceuticals, and inorganic salts. ACS Applied Materials & Interfaces, 9(46): 40369-40377. https://doi.org/10.1021/acsami.7b14217

[40] Abdolhosseinzadeh, S., Asgharzadeh, H., Seop Kim, H. (2015). Fast and fully-scalable synthesis of reduced graphene oxide. Scientific Reports, 5(1): 10160. https://doi.org/10.1038/srep10160

[41] Hayyan, M., Abo-Hamad, A., AlSaadi, M.A., Hashim, M.A. (2015). Functionalization of graphene using deep eutectic solvents. Nanoscale Research Letters, 10(1): 324. https://doi.org/10.1186/s11671-015-1004-2

[42] Sayehi, M., Sahnoun, R.D., Fakhfakh, S., Baklouti, S. (2018). Effect of elaboration parameters of a membrane ceramic on the filtration process efficacy. Ceramics International, 44(5): 5202-5208. https://doi.org/10.1016/j.ceramint.2017.12.127

[43] Qabaqous, O., Tijani, N., Bennani, M.N., El Krouk, A. (2014). Elaboration et caractérisation des supports plans à base d'argile (Rhassoul) pour membranes minérales (Preparation and characterization of supports plans from the (Rhassoul) Clay for mineral membranes). Journal of Materials and Environmental Science, 5: 2244-2249.

[44] Bousbih, S., Errais, E., Darragi, F., Duplay, J., Trabelsi-Ayadi, M., Daramola, M.O., Ben Amar, R. (2021). Treatment of textile wastewater using monolayered ultrafiltation ceramic membrane fabricated from natural kaolin clay. Environmental Technology, 42(21): 3348-3359. https://doi.org/10.1080/09593330.2020.1729242

[45] Thommes, M., Kaneko, K., Neimark, A.V., Olivier, J.P., Rodriguez-Reinoso, F., Rouquerol, J., Sing, K.S. (2015). Physisorption of gases, with special reference to the evaluation of surface area and pore size distribution (IUPAC Technical Report). Pure and Applied Chemistry, 87(9-10): 1051-1069. https://doi.org/10.1515/pac-2014-1117

[46] Zubir, N.A., Yacou, C., Motuzas, J., Zhang, X., Diniz da Costa, J.C. (2014). Structural and functional investigation of graphene oxide–Fe_3O_4 nanocomposites for the heterogeneous Fenton-like reaction. Scientific Reports, 4(1): 4594. https://doi.org/10.1038/srep04594

[47] Majoulet, O. (2012). Elaboration de céramiques poreuses ordonnées à base de carbure de silicium. Ph.D. dissertation. Université de Limoges, France. https://theses.hal.science/tel-00869142v1 accessed on Mar. 12, 2025.

[48] Cychosz, K.A., Thommes, M. (2018). Progress in the physisorption characterization of nanoporous gas storage materials. Engineering, 4(4): 559-566. https://doi.org/10.1016/j.eng.2018.06.001

[49] MCA Services. (2022). The origin of hysteresis in gas adsorption - desorption isotherms. https://www.youtube.com/watch?v=aBWGC1ICV6k, accessed on Mar. 12, 2025.

[50] L'isotherme d'adsorption. Qu'appelle-t-on isotherme d'adsorption (ou de désorption)? https://nte.mines-albi.fr/STP/fr/co/uc_IsothermeAdsorption.html.

[51] Karaman, S., Ersahin, S., Gunal, H. (2006). Firing temperature and firing time influence on mechanical and physical properties of clay bricks. Journal of scientific and industrial research, 65(2): 153-159. https://nopr.niscpr.res.in/bitstream/123456789/4811/1/JSIR%2065%282%29%20153-159.pdf.

[52] McDonald, M.P., Morozov, Y., Hodak, J.H., Kuno, M., Gao, W. (2015). Graphene Oxide: Reduction Recipes, Spectroscopy, and Applications. Springer Cham. https://doi.org/10.1007/978-3-319-15500-5

[53] Lavin-Lopez, M.D.P., Paton-Carrero, A., Sanchez-Silva, L., Valverde, J.L., Romero, A.J.A.P.T. (2017). Influence of the reduction strategy in the synthesis of reduced graphene oxide. Advanced Powder Technology, 28(12): 3195-3203. https://doi.org/10.1016/j.apt.2017.09.032

[54] Huang, H., Sun, G., Hu, J., Jiao, T. (2015). Low temperature synthesis of MnO_2/graphene nanocomposites for supercapacitors. Journal of Chemistry, 2015(1): 629362. https://doi.org/10.1155/2015/629362

[55] Liu, X., Yu, L., Liu, H., Chen, L., Li, L. (2008). In situ thermal decomposition of starch with constant moisture in a sealed system. Polymer Degradation and Stability, 93(1): 260-262.

https://doi.org/10.1016/j.polymdegradstab.2007.09.004
[56] Liu, X., Yu, L., Xie, F., Li, M., Chen, L., Li, X. (2010). Kinetics and mechanism of thermal decomposition of cornstarches with different amylose/amylopectin ratios. Starch-Stärke, 62(3-4): 139-146. https://doi.org/10.1002/star.200900202
[57] Alvarado, C., Alvarado-Quintana, H., Siche, R. (2023). Ceramic thermal insulator based on diatomite obtained by starch consolidation casting. Materials, 16(11): 4028. https://doi.org/10.3390/ma16114028
[58] Salman, M.M., Radhi, N.S., Sabr, O.H., Nhabih, H.T. (2020). Utilization of diverse cheap materials as pore generating agent to manufacture low-cost porous ceramic. Cerâmica, 66: 179-185. https://doi.org/10.1590/0366-69132020663782873
[59] Khattab, R.M., El-Rafei, A.M., Zawrah, M.F. (2018). Fabrication of porous TiO_2 ceramics using corn starch and graphite as pore forming agents. Interceram-International Ceramic Review, 67(4): 30-35. https://doi.org/10.1007/s42411-018-0024-1
[60] Huang, K., Wang, L., Li, M., Mi, T., Zhang, J., Liu, J., Yi, X. (2023). Mechanism of porous ceramic fabrication using second aluminum dross assisted by corn stalk as pore-forming agent. Environmental Technology & Innovation, 31: 103195. https://doi.org/10.1016/j.eti.2023.103195
[61] Biggemann, J., Stumpf, M., Fey, T. (2021). Porous alumina ceramics with multimodal pore size distributions. Materials, 14(12): 3294. https://doi.org/10.3390/ma14123294
[62] Nasir, N., Jumaidin, R., Selamat, M.Z., Salleh, S., Lau, K.T. (2015). Effect of different types of pore-forming agent on the macro pore size of ceramic. Applied Mechanics and Materials, 761: 380-384. https://doi.org/10.4028/www.scientific.net/AMM.761.380
[63] Zhao, J., Ban, X., Yang, Y., Yuan, Z., Ru, H., Su, D. (2023). Fabrication of SiC porous ceramics by foaming method. Materials, 16(4): 1342. https://doi.org/10.3390/ma16041342